P-Type Transparent Cu-Alloyed ZnS Deposited at Room Temperature

Rachel Woods-Robinson, Jason K. Cooper, Xiaojie Xu, Laura T. Schelhas, Vanessa L. Pool, Alireza Faghaninia, Cynthia S. Lo, Michael F. Toney, Ian D. Sharp, and Joel W. Ager III*

All transparent conducting materials (TCMs) of technological practicality are n-type; the inferior conductivity of p-type TCMs has limited their adoption. In addition, many relatively high-performing p-type TCMs require synthesis temperatures >400 °C. Here, room-temperature pulsed laser deposition of copper-alloyed zinc sulfide ($Cu_xZn_{1-x}S$) thin films ($0 \leq x \leq 0.75$) is reported. For $0.09 \leq x \leq 0.35$, $Cu_xZn_{1-x}S$ has high p-type conductivity, up to 42 S cm^{-1} at $x = 0.30$, with an optical band gap tunable from ≈3.0–3.3 eV and transparency, averaged over the visible, of 50%–71% for 200–250 nm thick films. In this range, synchrotron X-ray and electron diffraction reveal a nanocrystalline ZnS structure. Secondary crystalline Cu_yS phases are not observed, and at higher Cu concentrations, $x > 0.45$, films are amorphous and poorly conducting. Within the TCM regime, the conductivity is temperature independent, indicating degenerate hole conduction. A decrease in lattice parameter with Cu content suggests that the hole conduction is due to substitutional incorporation of Cu onto Zn sites. This hole-conducting phase is embedded in a less conducting amorphous Cu_yS, which dominates at higher Cu concentrations. The combination of high hole conductivity and optical transparency for the peak conductivity $Cu_xZn_{1-x}S$ films is among the best reported to date for a room temperature deposited p-type TCM.

1. Introduction

Transparent conducting materials (TCMs) are used in a wide range of applications including low emissivity ("low-e") windows, front electrodes in display technologies, and "smart" windows.[1–3] In recent years, TCMs have also become increasingly important in electronic and opto-electronic fields, including thin film photovoltaics, solid state and organic LED lighting, printed electronics, and organic electronics.[4–10] At present, all commercially implemented TCMs are n-type (electron conducting) and include Sn-doped In_2O_3 (ITO), F-doped SnO_2, and Al-doped ZnO.[3,4,10] Since the most widely utilized TCMs are oxides, the designation TCO, transparent conducting oxide, is commonly employed.

In contrast, p-type (hole conducting) TCMs (p-TCMs) are far less developed. There are a number of proposed applications for these materials, such as transparent emitter contacts for n-type solar cells, transparent interconnects for non-epitaxial tandem solar cells, contacts to light emitting diodes, and "invisible electronics."[11–17] However, none of these concepts have been realized due to limitations in the currently known materials systems. As such, an efficient photovoltaic device incorporating a p-type TCM has not yet been demonstrated.[18] The primary challenge in using p-TCMs in practical applications is performance, specifically the combination of hole conductivity and transparency.[15] Additionally, application of existing TCM materials to device stacks is further limited by the necessity for processing at temperatures greater than 400 °C for the highest performing layers currently available.

The first p-TCM, delafossite $CuAlO_2$, was reported in 1997,[14] and since that time there have been considerable research

R. Woods-Robinson, X. Xu, Dr. J. W. Ager III
Materials Sciences Division
Lawrence Berkeley National Laboratory
1 Cyclotron Road, Berkeley, CA 94720, USA
E-mail: jwager@lbl.gov

Dr. J. K. Cooper, Dr. I. D. Sharp, Dr. J. W. Ager III
Joint Center for Artificial Photosynthesis
Lawrence Berkeley National Laboratory
1 Cyclotron Road, Berkeley, CA 94720, USA

Dr. J. K. Cooper, Dr. I. D. Sharp
Chemical Sciences Division
Lawrence Berkeley National Laboratory
1 Cyclotron Road, Berkeley, CA 94720, USA

Dr. L. T. Schelhas, Dr. V. L. Pool, Dr. M. F. Toney
Stanford Synchrotron Radiation Lightsource
SLAC National Accelerator Laboratory
2575 Sand Hill Road, Menlo Park, CA 94025, USA

A. Faghaninia, Prof. C. S. Lo
Department of Energy
Environmental and Chemical Engineering
Washington University in St. Louis
Brauer Hall, CB 1180, 1 Brookings Drive
Saint Louis, MO 63130, USA

**ADVANCED
ELECTRONIC
MATERIALS**
www.advelectronicmat.de

*Materials
Views*
www.MaterialsViews.com

efforts to improve performance. Many oxides have been investigated including oxygen intercalated and doped Cu-delafossites with Al replaced by other metal cations such as Cr,[19] Fe,[20] Sc,[21] and Y,[22] ZnO-based TCOs such as N:In co-doped ZnO,[23] spinel structure TCOs such as $NiCo_2O_4$,[24,25] and amorphous oxides such as $ZnO·Rh_2O_3$ and MoO_3.[26,27] However, the performance of p-TCMs remains inferior by orders of magnitude compared to that of n-TCMs. For example, while state-of-the-art 100 nm thick ITO can have a conductivity approaching 10 000 S cm^{-1}, sheet resistance <10 Ω sq^{-1}, and a transmittance in the visible of >80%, the best reported combination of conductivity and transparency for a p-type TCM is for Cu_2O-doped $Zn_{1-x}Al_xO$ with σ = 144 S cm^{-1} and 80%–85% optical transparency.[28] Typical performance metrics for state-of-the-art p-type TCMs (see Table S1 for details, Supporting Information) are conductivity in the range 1–250 S cm^{-1}, sheet resistance >200 Ω sq^{-1}, and transparencies less than 80%.

The processing conditions used to synthesize p-TCMs also limit their applications. All relatively high performing p-TCMs require processing temperatures of 400 °C or greater (Table S1, Supporting Information). For example, the Cu_2O-doped $Zn_{1-x}Al_xO$ films mentioned previously require a 400 °C anneal in N_2 and H_2 gas to achieve high conductivity.[28] This again contrasts with n-TCMs, for which room temperature syntheses have been developed,[6,29,30] enabling application of these materials in device stacks with limited thermal budgets such as thin film photovoltaics, organic photovoltaics, and flexible electronics.[10,31] For p-TCMs, there are only a few reports of room temperature deposition including $ZnO·Rh_2O_3$ and Zn-Co-O with conductivities of 1.9 and 21 S cm^{-1}, respectively;[26,32] in these studies p-type conductivity was reported but the band gaps are in the visible range, leading to reduced optical transmission. Furthermore, in the case of $ZnO·Rh_2O_3$, the incorporation of the rare element Rh is undesirable for most TCM applications, which typically require large-scale production with low cost.

While the optical transparency of wide band gap oxides make them a good starting point for investigation of new p-TCMs, the localized character of the valence band, which is formed by oxygen 2p orbitals, presents a fundamental challenge.[14] This was examined recently in the computational screening work of Hautier et al.[15] which found that the vast majority of the metal oxides have valence band maximum (VBM) effective masses much larger than 1 m_e, leading to a prediction of low hole mobility. Interestingly, it was found in some cases that the incorporation of S as a second anion could function to delocalize the VBM, leading to predictions of lower VBM effective masses and, potentially, higher hole mobility. Indeed, there are a few literature reports of relatively good p-TCM performance achieved using non-oxide chalcogenide-based p-TCMs such as $CuAlS_2$ and $BaCu_2(S, Se)F$.[33–35]

Here we report the room temperature synthesis of a highly conductive and transparent p-type TCM. We use, as a starting point, ZnS, which is a wide-band gap semiconductor. The low-temperature phase of ZnS is typically cubic (β zinc-blende, or sphalerite) with a band gap of ≈3.7 eV, and the high-temperature hexagonal (α wurtzite) phase has a band gap of 3.9 eV.[36] Cu substituted onto Zn sites should function as acceptors and generate free holes. Cu doping and alloying into both phases

of ZnS at low concentrations has been previously explored in thin films[37–41] and nanoparticles,[42,43] particularly for electroluminescent applications and with some reports of p-type character; studies have shown Cu to be sparingly soluble up to about 0.06% in zinc-blende ZnS in equilibrium.[44–46] In prior work, we synthesized copper-alloyed wurtzite $Cu_xZn_{1-x}S$ films with x up to 0.26 at elevated temperature (550 °C). The films exhibited p-type conductivity and optical transparency in the visible range.[47] Here we show that $Cu_xZn_{1-x}S$ films can be synthesized at room temperature by pulsed laser deposition (PLD), and investigate the structure and conductivity mechanism in greater detail. At an optimal Cu concentration of $x = 0.30$, the hole conductivity reaches 42 S cm^{-1} and the material retains high optical transparency. The combination of hole conductivity and optical transparency of $Cu_xZn_{1-x}S$ is, to our knowledge, the best reported to date for a room temperature deposited p-type TCM. Room temperature synthesis of p-TCMs should enable their use in technological applications requiring a low thermal budget and will allow for new optoelectronic device architectures.

2. Results

2.1. Sample Preparation, Composition, and Morphology

Thin films of Cu-alloyed ZnS were synthesized by PLD, using $ZnS:Cu_2S$ targets. Extra S powder was added to produce a target stoichiometry of $Cu_xZn_{1-x}S_{1.0}$ (0 ≤ x ≤ 0.75). Films were deposited on quartz substrates at room temperature. Rutherford backscattering spectroscopy (RBS) was used to determine sulfur content and particle-induced X-ray emission (PIXE) was selected to assess the Cu:Zn ratio (see the Experimental Section). The cation stoichiometry in the films mirrored the target stoichiometry by ±2%. Films were slightly sulfur deficient compared to targets. The sulfur content was 0.90 < z < 0.95 (with notation $Cu_xZn_{1-x}S_z$) for x < 0.45, but for x > 0.45 dropped to $z = 0.75$ at $x = 0.75$ (cf. Figure S4, Supporting Information). Films are reported herein as $Cu_xZn_{1-x}S$ to emphasize the cation stoichiometry. Additionally, control films from Cu_2S and CuS targets were synthesized.

The presence of crystalline phases in $Cu_xZn_{1-x}S$ films was investigated carefully by synchrotron wide-angle X-ray scattering (WAXS). As shown in **Figure 1**, broad diffraction peaks were observed for all 0 ≤ x ≤ 0.45 films at approximately Q = 1.90, 2.00, 3.30, and 3.85 Å^{-1}. The latter three peaks can be indexed to either the (111), (220), and (311) zinc-blende (β) ZnS lattice planes or the (002), (110), and (112) wurtzite (α) ZnS planes, as discussed below. The peak at $Q = 1.90$ Å^{-1} can be uniquely assigned to the (100) plane of wurtzite. Films with x ≈ 0.45 have only weak peaks, and ZnS crystallinity is completely lost with x > 0.45. For higher Cu content ($x = 0.75$), no peaks are observed and the films are amorphous. Films made from Zn-free Cu_2S and CuS targets (black and grey traces in Figure 1) have weak crystalline peaks assignable to $Cu_{1.8}S$ and CuS, respectively.

Discrimination of the wurtzite (α) and zinc-blende (β) crystalline phases of ZnS requires care, as many of the expected peaks overlap. Therefore, to determine the phase of the film the data were compared to literature powder patterns, which
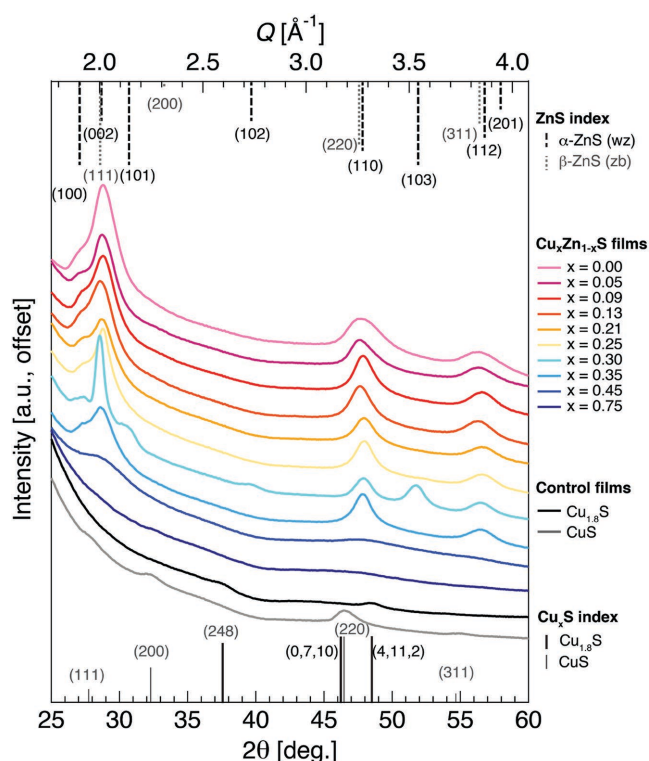
Figure 1. Wide-angle X-ray scattering (WAXS) diffraction patterns of $Cu_xZn_{1-x}S$ films deposited on quartz at room temperature for $0 \leq x \leq 0.75$. Spectra are plotted versus Q (upper x-axis) and against the equivalent Cu Kα 2θ diffraction angle (lower x-axis). Films contain a mix of wurtzite (wz, α) and zinc-blende (zb, β) ZnS. Vertical lines correspond to diffraction standards of the indicated crystal phases from the ICDD powder diffraction database.[59] The control films from the zinc-less targets are nanocrystalline $Cu_{1.8}S$ (black trace, from Cu_2S target) and CuS (grey trace, from CuS target), but no copper sulfide peaks are observed in the $Cu_xZn_{1-x}S$ films. The background signal is from the quartz substrate.

Figure 2. Selected area electron diffraction (SAED) patterns of a) a $Cu_xZn_{1-x}S$ film with $x = 0.45$. The observed rings are assigned in the figure to (111), (220), and (311) from β-ZnS, but could also be from the closely overlapping α peaks (see Figure 1). b) SAED pattern from a $Cu_{1.8}S$ control film with the indicated indexing. No crystalline Cu-containing phases were observed from the $x = 0.45$ film shown in panel (a).

are shown schematically in Figure 1. In $Cu_xZn_{1-x}S$ films, the β-(111) peak is the strongest peak observed, while for the wurtzite structure the α-(002) peak is weaker than the α-(101) peak. Thus, the strong intensities of the peaks near $Q = 2.0$ Å^{-1} suggest the β-ZnS phase is present. However, the unique α-(100) peak appears in all $0 \leq x \leq 0.35$ films as a shoulder at $Q = 1.9$ Å^{-1}. Also, $x = 0.30$ films reproducibly have observable α peaks at (101), (102), and (103). Thus, $Cu_xZn_{1-x}S$ films with crystalline WAXS peaks contain a mixture of wurtzite (α) and zinc-blende (β) phases with a high level of disorder. A Scherrer analysis of the β-(220)/α-(110) ZnS peaks suggest a coherence length of approximately 3–6 nm (details in Supporting Information, Figure S5), and this was found to increase slightly with x up to $x \leq 0.35$, and then drop significantly at $x = 0.45$.

The nature of the crystalline phases in the films was further examined by electron diffraction. **Figure 2**a shows a selected area electron diffraction (SAED) pattern for a film with $x = 0.45$, which is a composition with less crystalline ZnS compared to lower Cu contents. Consistent with the WAXS data from Figure 1, the (111), (220), and (311) rings due to zinc-blende ZnS are observed (or the closely overlapping (002), (110), and (112) from wurtzite ZnS). Neither Cu_yS nor elemental Cu phases are observed. The SAED pattern from an $x = 0.30$ film
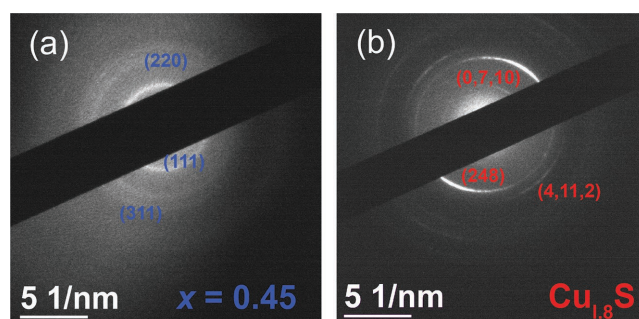
is Figure S6 (Supporting Information); again, overlapping rings due to α- and β-ZnS are observed, and no crystalline Cu-phases are present. For comparison, the pattern from a control Cu_2S film is shown in Figure 2b. The (0,7,10), (216), and (4,11,2) rings of Cu_2S are observed and are consistent with the black trace in Figure 1.

Since copper is a smaller cation than zinc, we expect its substitution for Zn in the ZnS lattice would decrease the lattice parameter and yield a peak shift to higher Q. **Figure 3**a shows the position of the α-(100) peak for $Cu_xZn_{1-x}S$ for $0 \leq x \leq 0.45$; this peak does not overlap with any of the β peaks, allowing for quantitative analysis. Upon Cu incorporation the peak shifts to higher Q values with the maximum shift observed at $x \geq 0.25$. The corresponding value of the lattice parameter a is shown in Figure 3b. The shift is not entirely monotonic but saturates near $x = 0.21$, corresponding to a lattice parameter contraction of -1.5% with respect to the ZnS control film. We estimated the shift expected for complete Cu substitution into the ZnS lattice using ab initio calculations (see Supporting Information for details). The values, which monotonically decrease with increasing Cu concentration, are also plotted in Figure 3b. The Cu content at which the lattice shift saturates corresponds to the calculated shift at $x \approx 0.2$. While not definitive, we conclude that there is a maximum of about 20% incorporation of Cu into the wurtzite phase. Due to peak overlaps, it was not possible to perform a similar analysis for the zinc-blende peaks, but it is conceivable that there is Cu substitution into this phase, as well.

Although no crystalline Cu_yS phases in the $Cu_xZn_{1-x}S$ films were apparent from WAXS measurements, characteristic micro-Raman peaks in PLD films with $x \geq 0.13$ are found in **Figure 4** to lie around 470–480 cm^{-1} and coincide with covellite CuS and aninite Cu_7S_4.[48] These features suggest that a nanocrystalline Cu_yS phase forms with significant Cu incorporation. However, in each film the presence, strength, and location of these peaks vary significantly with lateral position, suggesting a strong spatial dependence of Cu_yS. This indicates that the Raman signal could be from surface nucleation of Cu_yS, as shown in the SEM image in Figure S3 (Supporting Information), rather than from bulk phases. It is also possible that $Cu_xZn_{1-x}S$ in the zinc-blende phase may have peaks in this vicinity due to two-mode behavior of the Raman modes in this alloy system.

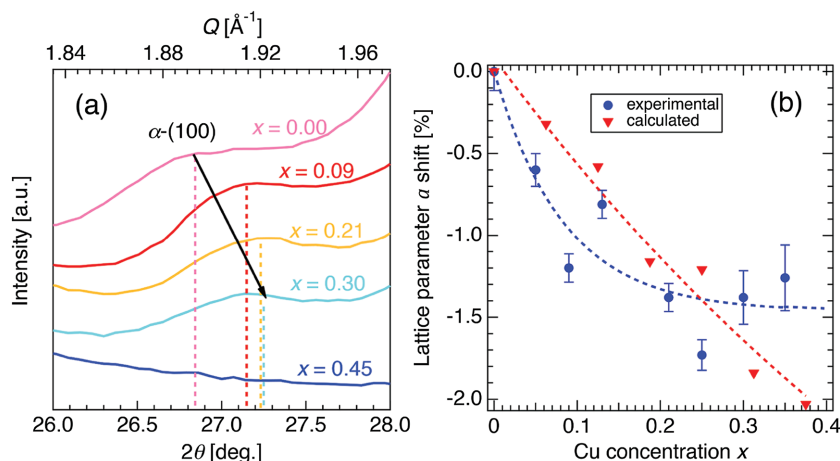**Figure 3.** a) A subset of Figure 1, illustrating a shift of the α-ZnS (100) crystal peak to higher Q for five representative films. Dotted lines correspond to peak centers, as determined by a fit to a Voigt and linear background subtraction. b) The corresponding lattice constant a as a function of Cu concentration (blue circles). Error bars are the standard deviation of the Voigt fit. Red triangles are the expected theoretical lattice shifts for complete Cu substitution from ab initio calculations (see the Supporting Information). Dashed lines are guides for the eye.

2.2. Electronic Properties

Conductivity of the $Cu_xZn_{1-x}S$ films is shown as a function of Cu concentration in **Figure 5**. All films with $x > 0$ were found to be p-type conductors, as indicated by positive Seebeck coefficients (Figure 5 inset and Figure S9a, Supporting Information). Conductivity increases gradually up to $x = 0.30$ and then decreases drastically, which tracks the loss of ZnS crystallinity

in films with $x > 0.35$ as shown in Figure 1. At a given Cu concentration, conductivities appear to have no correlation to the sulfur concentration in films (Figure S4, Supporting Information). A maximum conductivity of 42 S cm^{-1} is found in films with $x = 0.30$. We identify a "TCM regime" in the approximate range $0.09 \leq x \leq 0.35$, where films reproducibly have conductivities over 10 S cm^{-1}. The properties of films in this range are summarized in **Table 1**.

Hall effect measurements were used to estimate the hole concentration, p, and hole mobility, μ_h. Hole concentrations in the peak conductivity films ($x = 0.30$) are $1.8 \pm 0.1 \times 10^{20}$ cm^{-3}. As shown in Figure 5, p increases gradually with Cu concentration, peaks near $x = 0.35$, and then decreases quickly. Within the TCM regime, p varies from $1–2 \times 10^{20}$ cm^{-3}, which is in the range of a degenerately doped semiconductor. The values of p are consistent with Seebeck coefficient, as discussed in the Supporting Information. Films with $x = 0.30$ have mobilities of 1.4 ± 0.1 cm^2 V^{-1} s^{-1}, and within the range $0.25 \leq x \leq 0.35$ the hole mobility is greater than 1.0 cm^2 V^{-1} s^{-1}.

Figure 4. Micro-Raman spectra obtained from $Cu_xZn_{1-x}S$ films. Raman powder standards of crystalline phases of Cu_yS and ZnS are from the RRUFF project.[48] It should be noted that within a given film, the spectra had a large dependence on lateral position and peaks were not always observed (see the text).
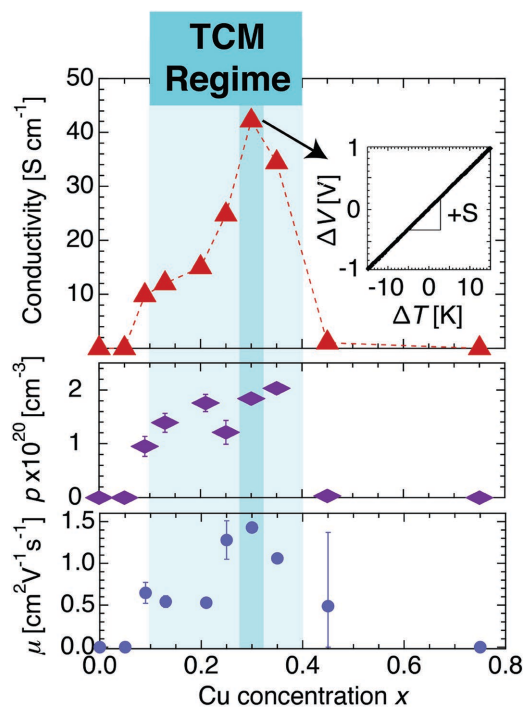

Figure 5. Measurements of conductivity (top), hole concentration (middle), and mobility (bottom), as a function of Cu content (x) for $Cu_xZn_{1-x}S$ films ($0 \leq x \leq 0.75$). The maximum conductivity, 42 S cm^{-1}, is observed at $x = 0.30$. A Seebeck coefficient measurement of this film is shown in the inset, and Seebeck coefficients over the full range of x are plotted in Figure S12 in the Supporting Information. Error bars in p and μ are calculated from the statistical variation in Hall effect measurements with applied currents ranging over five orders of magnitude.

Table 1. Electronic and optical properties of room temperature deposited $Cu_xZn_{1-x}S$ films in the "TCM regime" ($0.09 < x < 0.35$), with $x = 0$ and $x = 0.45$ films shown for reference. The film with the highest conductivity ($x = 0.30$) is highlighted.

x	Thickness [nm]	Conductivity [S cm^{-1}]	Sheet resistance [$\Omega\,\square^{-1}$]	Hole concentration [$\times 10^{20}$ cm^{-3}]	Mobility [cm^2 v^{-1} s^{-1}]	Seebeck coefficient [uV K^{-1}]	Optical band gap [eV][a]	Avg. visible T [%][b]
0	149	N/A	N/A	N/A	N/A	N/A	3.3	85.8
0.09	325	9.8	3135	1.0 ± 0.2	0.65 ± 0.13	60.0	3.4	70.9
0.13	257	12.0	3231	1.4 ± 0.2	0.54 ± 0.07	59.0	3.35	68.1
0.21	226	14.8	2985	1.8 ± 0.2	0.53 ± 0.05	66.5	3.22	59.2
0.25	224	24.8	1805	1.2 ± 0.2	1.28 ± 0.23	67.9	3.25	59.3
0.30	218	42.2	1089	1.8 ± 0.7	1.43 ± 0.05	63.5	3.13	51.7
0.35	244	34.4	1194	2.0 ± 0.1	1.06 ± 0.06	60.2	3.1	50.0
0.45	230	0.25	171 000	N/A	N/A	147	2.8	47.7

[a]Extrapolated from Figure 7c; [b]Average optical transmittance (400–800 nm) is measured with UV-vis spectrophotometry. Reflectance is about 15% (see the Supporting Information), but, in an actual device, texturing or antireflective coatings would be used to push reflectance to zero. Based on our ellipsometry measurements, in such case higher T is possible, e.g., almost 70% for the $x = 0.30$ film.

2.3. Temperature Dependence of Conductivity

The conductivity was measured in the range of 15–400 K for four representative films ($x = 0.09, 0.21, 0.30, 0.45$), as shown in **Figure 6**. In films $x = 0.09$, 0.21, and 0.30, the conductivity decreases only very slightly below room temperature and essentially plateaus at a constant value, suggesting degenerate hole conduction within the valence band. This behavior is similar to metallic conduction in other p-type transparent sulfides, such as doped $CuAlS_2$,[33,34,49,50] but contrasts with the activated transport mechanisms typical in oxide-based TCMs (cf. Table S1, Supporting Information).[14,19–22,32,51] Outside of the TCM regime, for example in the $x = 0.45$ sample, conductivity decreases by nearly three orders of magnitude at low temperatures, indicating an activated transport mechanism with low conductivity at room temperature (0.25 S cm^{-1}).

2.4. Optical Properties

All room temperature deposited $Cu_xZn_{1-x}S$ films with $x \geq 0.45$ (thicknesses of 200–250 nm) are optically transparent. The
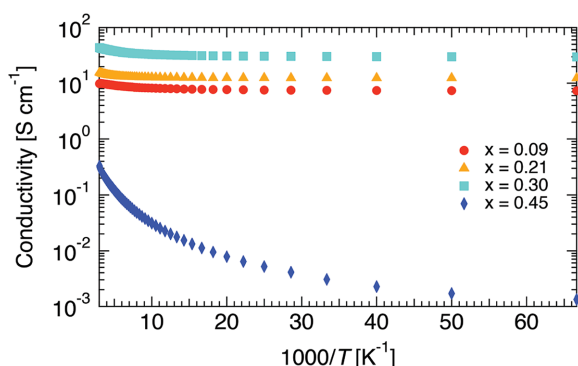

Figure 6. Temperature dependence of hole conductivity is shown for $Cu_xZn_{1-x}S$ films. The near constant conductivity profiles at low temperatures (high 1000/T) for $x = 0.09$, 0.21, 0.30 suggest degenerate doping, as expected, and metallic-like band conduction. In contrast, the $x = 0.45$ film appears to have an activated transport mechanism.

transparency was found to decrease monotonically with increasing copper content, as plotted in **Figure 7**a, in part due to a shift in the optical band gap at higher Cu concentrations. After correcting for the transmittance of the quartz substrate and evaluating UV-vis transmission data in the spectral range of 400–800 nm, it was found that $x = 0$ films have an average optical transparency of approximately 86%, while films with $x = 0.09$, 0.21, and 0.30 have average transparencies of 71%, 60%, and 52% (see details in the Supporting Information). The large reflection fringes from the air-film, film-quartz and quartz-air interfaces are found to oscillate between around 5%–40% for each film (cf. Figure S14, Supporting Information). Transparencies of these 200–250 nm thick films without reflectance from the interfaces are derived from ellipsometry measurements, and we show that transparency could be improved by up to 15% by minimizing reflection losses. Thus, transparency of the $x = 0.30$ film could be improved from 52% to 65% with application of a suitable antireflection coating, and transmission values that are corrected to account for reflection losses of other films in the "TCM regime" are provided in the Supporting Information (cf. Figure S16a, Supporting Information).

In order to examine the inherent tradeoff between conductance and transparency, the effect of film thickness on transparency, which is affected by reflection and thin film interference losses, was studied for films with the highest conductivity ($x = 0.30$). As shown in Figure 7b, 80 nm thick films are over 65% transparent on average in the visible spectrum and ≈65% transparent at 550 nm. Films as thick as 250 nm were shown to be at least 60% transparent at 550 nm and over 50% on average in the visible spectrum. Beyond this thickness, the transparency decreases exponentially with film thickness.

By fitting variable angle spectroscopic ellipsometry (VASE) data, as described in the Supporting Information, we determined the absorption coefficient as a function of composition. These results were used to generate Tauc plots and to estimate the apparent optical gap as a function of copper concentration, as shown in Figure 7c. The optical band gap varies with composition from about 3.3 eV in the undoped film ($x = 0$) to about 2.5 eV in the films with $x = 0.45$. The optical band gap at $x = 0.35$, the composition with the second highest conductivity measured,
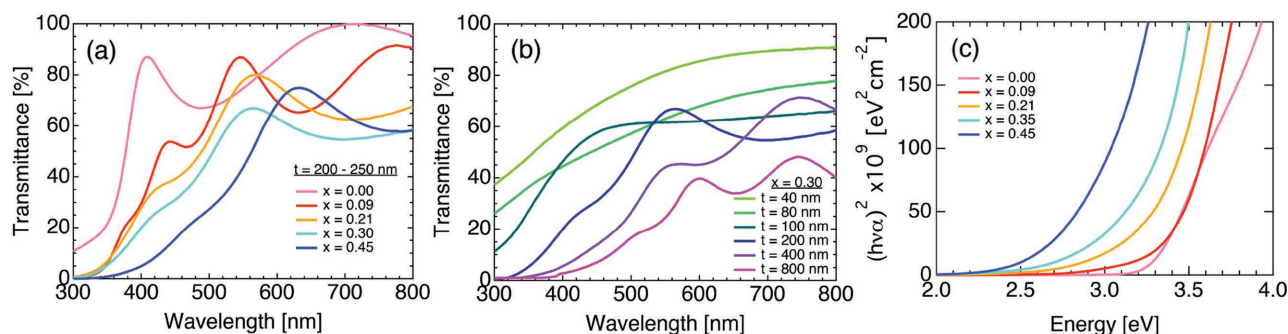
Figure 7. a) Transmittance as a function of Cu concentration (*x*) and b) transmittance as a function of film thickness (*t*), both normalized to remove the average absorbance from the quartz substrate. Fringes are due to reflectance from the quartz and air interfaces. (c) Tauc plots derived from ellipsometric measurements of the absorption coefficient are used to estimate the optical band gap as a function of *x*. Optical band gaps in room temperature deposited films are shown to vary from ≈2.5 to 3.3 eV.

was ≈3.1 eV. This is the limit at which TCMs are still considered "transparent."[12] The incorporation of Cu into the ZnS lattice should not introduce mid-gap states or significantly shrink the gap for wurtzite or zinc-blende ZnS, as shown by partial density of states calculations in the Supporting Information. At $x = 0.09$, the absorption is still quite low. But as we ramp the Cu content ($x > 0.35$), absorption from Cu_yS phases, which have smaller band gaps (0.6–2.35 eV, depending on crystal structure),[52] begins to dominate and significantly decrease transmittance. Additionally, band tailing might be present at low Cu concentrations.

3. Discussion

$Cu_xZn_{1−x}S$ films synthesized in this study incorporate up to 20% Cu into the crystalline ZnS lattice. In prior reports, the solubility of Cu in zinc-blende ZnS saturates at <0.1%, above which Cu_yS precipitates form.[43,44] We attribute the higher Cu incorporation achieved here to the ability of PLD to stabilize metastable phases due to nonequilibrium laser ablation and rapid quenching on the substrate.[53] As one example, in the similar ternary system $Mg_xZn_{1−x}O$, incorporation of Mg up to 33%, far above the equilibrium solubility limit, has been reported.[54,55]

In this context, the conductivity as a function of Cu concentration (Figure 5) is interesting. One might find it somewhat counterintuitive that $Cu_xZn_{1−x}S$ films with larger Cu contents have low hole conductivity, given that films made under the same condition using CuS and Cu_2S target have conductivities of 2,100 S cm$^{−1}$ and 680 S cm$^{−1}$, respectively. If Cu_yS phases were contributing significantly to the conductivity, we would expect the conductivity to increase monotonically as a function of *x*. Instead, hole conductivity peaks near $x = 0.30$, drops to <1 S cm$^{−1}$ at $x = 0.45$ and is negligible at $x = 0.75$. Moreover, we were not able to observe any crystalline Cu_yS phases by either x-ray or electron diffraction, implying that Cu_yS phases (and, possibly a Zn-doped Cu_yS phase at higher Cu contents) present are amorphous.

A model that is consistent with the observed structural and electronic data is as follows. In the TCM regime, the PLD process produces a multiphase material. The lattice constant shift and the appearance of hole conductivity are evidence for some substitutional Cu incorporation into the crystalline ZnS phases

with the remaining Cu in an amorphous Cu_yS phase. If Cu occupies a Zn site as a +1 ion (as shown by XANES and XPS, cf. Supporting Information), it should function as an acceptor, producing free holes.[47,56] The connectivity of the hole-conducting phase is such that conductivity is independent of temperature. Conductivity increases with increasing Cu substitution until its maximum at $x = 0.30$. Formation of crystalline ZnS phases is suppressed at $x ≈ 0.45$ and higher; conduction mechanism changes to activated hopping and the conductivity at room temperature drops significantly. Eventually, at higher Cu contents, crystalline phases are not formed and the $Cu_xZn_{1−x}S$ films have low conductivity. The measured drop in sulfur concentration *z* with increasing *x* is consistent with this explanation (see the Supporting Information, Figure S4).

To simultaneously compare the performance and the synthesis conditions of the $Cu_xZn_{1−x}S$ films in this study with literature reports of high-performing p-type TCMs, we plot the conductivity against the processing temperature in **Figure 8**. Details of selected films from the literature are listed in Table S1 (Supporting Information); the conductivities of these films range from 1–400 S cm$^{−1}$. The average optical absorption coefficient (between 400 nm and 800 nm) is estimated from transparency and film thickness measurements, as described in the Supporting Information, and is indicated by the color bar. The films selected for the figure represent the highest performing p-type TCMs to date known to the authors. The $Cu_xZn_{1−x}S$ films from this study have a higher combined conductivity and transparency than prior reports of p-type TCMs synthesized at room temperature, and, moreover, at less than 400 °C.

4. Conclusions

In summary, a series of copper-alloyed zinc sulfide ($Cu_xZn_{1−x}S$) films were deposited at room temperature using PLD. We investigated films across a wide range of Cu concentrations ($0 ≤ x ≤ 0.75$), and found an optimal "TCM regime"—with conductivities greater than 10 S cm$^{−1}$ and band gaps around 3.0 eV or greater—to be within the approximate range $0.09 ≤ x ≤ 0.35$. The highest conductivity, 42 S cm$^{−1}$, was achieved in films with $x = 0.30$, and with an optimal antireflection coating could have average transparencies up to 65%.
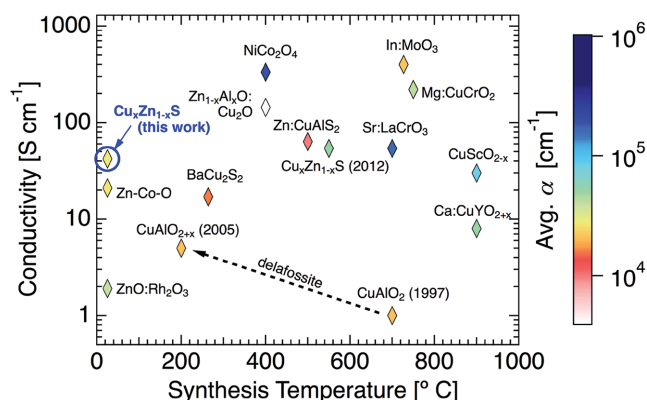
Figure 8. Conductivity plotted against maximum processing temperature for the highest performing $Cu_xZn_{1-x}S$ films of this study ($x = 0.30$, circled in blue) and for a group of the highest performing p-type TCM films in the literature, as reported in Table S1 in the Supporting Information.[14,19,21,22,27,28,34,51,60–62] The y-axis is the highest temperature reached during synthesis (either deposition or annealing). The color scale represents increasing absorption coefficient (averaged over 400–800 nm), with white the lowest (most transparent) and blue the highest (least transparent).

Films in the "TCM regime" have degenerate, temperature independent, hole conductivity. Within this range, WAXS and SAED showed films to be crystalline, predominantly in the zinc-blende ZnS phase, but showed no evidence of crystalline Cu_yS phases. We conclude it is likely that Cu is both (1) doping onto Zn sites to form a conductive phase and (2) phase separating into non-conductive amorphous Cu_yS. While development of a scalable synthesis method remains as a challenge, the combination of high p-type conductivity, high transparency, and a room temperature synthesis method for Cu-alloyed ZnS may enable new device applications, such as top electrodes for solar cells with n-type emitters, Ohmic contacts to p-type PV materials in device stacks with low thermal budgets (e.g. CdTe, CIGS, or CZTS), and transparent top contacts for light emitting diodes. Ultimately, such materials may allow for development of new optoelectronic architectures, including a number of "invisible electronics" concepts.[57]

5. Experimental Section

Synthesis: $Cu_xZn_{x-1}S$ films were synthesized using PLD in an SVTA SMART Nanotool PLD system. 1 in. diameter targets were made from Cu_2S, ZnS, and S powders by cold isostatic pressing at stoichiometric ratios of $x = Cu/(Cu+Zn) = 0$, 0.05, 0.10, 0.15, 0.20, 0.25, 0.30, 0.35, 0.45, and 0.75. Standard CuS and Cu_2S targets were synthesized as well. Prior to deposition, 1×1 cm^2 substrates of glass and quartz were cleaned in deionized water, acetone and O_2 plasma for 5 min. The chamber was pumped to a base pressure of 5×10^{-7} Torr for film growth. The laser source, a Coherent COMPexPro pulsed KrF excimer laser operating at 284 nm, was set at 10 ns pulse width, 10 Hz repetition rate, and 150 mJ pulse energy. Laser energy was carefully calibrated to account for systematic energy losses. The beam was directed through a spherical lens and a slit, focused to a 1.5 cm line, and swept across the target as it rotated. All depositions of this study were done at room temperature without substrate heating. Substrates were placed ≈5 cm from the target and spun at 2 RPM during deposition to achieve maximum uniformity. In situ film thickness was monitored with an SQM-160 quartz crystal microbalance.

Characterization: Film composition and thickness were determined using an RBS and combined in-situ PIXE system driven by an NEC model 5SDH Pelletron tandem accelerator. The S content was determined by RBS. PIXE was used to assess the Cu:Zn ratio because Cu and Zn backscattered energy peaks overlap in RBS. Peak fitting for PIXE was performed with Igor Pro software. Copper concentration in films was found to vary stoichiometrically with copper concentration in precursor PLD targets (with an error of ±0.02, accounting for precision and accuracy).[58]

The film structure was analyzed with WAXS on Beamline 11–3 at the Stanford Synchrotron Radiation Lightsource (SSRL). 2D scattering was collected with a MAR345 image plate at grazing incidence at an incident energy of 12.7 keV. Diffraction patterns were integrated between $5° < \chi < 175°$ for general analysis, $60° < \chi < 120°$ for lattice shift analysis, and $90° < \chi < 95°$ for Scherrer analysis. All peaks were fitted to Voigt line shapes with linear backgrounds. SAED was performed on a JEM-2100 LaB6 transmission electron microscope. Peak assignments for WAXS and SAED were made using the ICDD powder diffraction database.[59] Micro-Raman spectroscopy was performed with 532 nm laser excitation using a Horiba LabRam HR microscope.

Room temperature conductivity, mobility, and carrier concentration were measured using the van der Pauw contact configuration with an Ecopia HMS-3000 Hall Measurement System equipped with a 0.58 T magnet. Conductivity type was confirmed and Seebeck coefficient was determined using a thermopower measurement probe (see the Supporting Information for details). To measure conductivity as a function of temperature, a four-point probe was connected to a cryostat system with cooling and heating capabilities from 15–500 K.

Optical properties were measured with a SolidSpec 3000 UV–vis spectrophotometer operating with transmission and diffuse specular reflectance collected ⊥ and 17.5°, respectively. Reflectance measurements were referenced to freshly packed BaSO$_4$. Absorption coefficients were determined by VASE over the spectral range of 200–1600 nm, J. A. Woollam Co. M-2000 Ellipsometer. The reflection intensity was calibrated to a 25 nm SiO$_2$ on Si wafer. Fitting of both the ellipsometry data as well as transmission and reflection intensities was performed with CompleteEASE, in which a B-spline model with KK constraints was employed. Goodness of fit was determined by the mean squared error. Sample thickness determined by this method was in excellent agreement (≈3%–5%) with the RBS results.

Supporting Information

Supporting Information is available from the Wiley Online Library or from the author.

[1] C. Schaefer, G. Bräuer, J. Szczyrbowski, *Surf. Coat. Technol.* **1997**, *93*, 37.

[2] G. Bräuer, *Surf. Coat. Technol.* **1999**, *112*, 358.

[3] R. G. Gordon, *MRS Bull.* **2000**, *25*, 52.

[4] D. S. Ginley, C. Bright, *MRS Bull.* **2000**, *25*, 15.

[5] C. G. Granqvist, *Sol. Energy Mater. Sol. Cells* **2007**, *91*, 1529.

[6] H. Hosono, *Thin Solid Films* **2007**, *515*, 6000.

[7] W. Beyer, J. Hüpkes, H. Stiebig, *Thin Solid Films* **2007**, *516*, 147.

[8] E. Fortunato, D. Ginley, H. Hosono, D. C. Paine, *MRS Bull.* **2007**, *32*, 242.

[9] A. Klein, C. Körber, A. Wachau, F. Säuberlich, Y. Gassenbauer, S. P. Harvey, D. E. Proffit, T. O. Mason, *Materials* **2010**, *3*, 4892.

[10] K. Ellmer, *Nat. Photonics* **2012**, *6*, 809.

[11] D. L. Young, M. Contreras, M. Romero, S. Asher, C. Perkins, T. Gessert, J. Keane, T. J. Coutts, R. Noufi, in *Proc. 3rd World Conf. Photovolt. Energy Conversion*, WCPEC–3, Osaka, **2003**, *1*, 30.

[12] A. N. Banerjee, K. K. Chattopadhyay, *Prog. Cryst. Growth Charact. Mater.* **2005**, *50*, 52.

[13] S. Sheng, G. Fang, C. Li, S. Xu, X. Zhao, *Phys. Status Solidi A* **2006**, *203*, 1891.

[14] H. Kawazoe, M. Yasukawa, H. Hyodo, *Nature* **1997**, *289*, 939.

[15] G. Hautier, A. Miglio, G. Ceder, G.-M. Rignanese, X. Gonze, *Nat. Commun.* **2013**, *4*.

[16] J. F. Wager, *Science* **2003**, *300*, 1245.

[17] H. Ohta, M. Hirano, K. Nakahara, H. Maruta, T. Tanabe, M. Kamiya, T. Kamiya, H. Hosono, *Appl. Phys. Lett.* **2003**, *83*, 1029.

[18] A. E. Delahoy, S. Guo, in *Handbook of Photovoltaic Science and Engineering*, pp. 716–796 (Eds: A. Luque, S. Hegedus), John Wiley & Sons, Ltd., Weinheim, Germany **2011**.

[19] R. Nagarajan, A. D. Draeseke, A. W. Sleight, J. Tate, *J. Appl. Phys.* **2001**, *89*, 8022.

[20] C. Ruttanapun, W. Prachamon, A. Wichainchai, *Curr. Appl. Phys.* **2012**, *12*, 166.

[21] N. Duan, a. W. Sleight, M. K. Jayaraj, J. Tate, *Appl. Phys. Lett.* **2000**, *77*, 1325.

[22] R. Manoj, M. Nisha, K. A. Vanaja, M. K. Jayaraj, *Bull. Mater. Sci.* **2008**, *31*, 49.

[23] J. M. Bian, X. M. Li, X. D. Gao, W. D. Yu, L. D. Chen, *Appl. Phys. Lett.* **2004**, *84*, 541.

[24] C. F. Windisch, G. J. Exarhos, K. F. Ferris, M. H. Engelhard, D. C. Stewart, *Thin Solid Films* **2001**, *399*, 45.

[25] P. F. Ndione, Y. Shi, V. Stevanovic, S. Lany, A. Zakutayev, P. A. Parilla, J. D. Perkins, J. J. Berry, D. S. Ginley, M. F. Toney, *Adv. Funct. Mater.* **2014**, *24*, 610.

[26] S. Narushima, H. Mizoguchi, K. Shimizu, K. Ueda, H. Ohta, M. Hirano, T. Kamiya, H. Hosono, *Adv. Mater.* **2003**, *15*, 1409.

[27] H.-Y. Chen, H.-C. Su, C.-H. Chen, K.-L. Liu, C.-M. Tsai, S.-J. Yen, T.-R. Yew, *J. Mater. Chem.* **2011**, *21*, 5745.

[28] K. N. Hui, K. S. Hui, L. Li, Y. R. Cho, J. Singh, *Mater. Res. Bull.* **2013**, *48*, 96.

[29] S. Laux, N. Kaiser, A. Zöller, R. Götzelmann, H. Lauth, H. Bernitzki, *Thin Solid Films* **1998**, *335*, 1.

[30] F. Kurdesau, G. Khripunov, A. F. da Cunha, M. Kaelin, A. N. Tiwari, *J. Non-Cryst. Solids* **2006**, *352*, 1466.

[31] F. C. Krebs, M. Jørgensen, *Sol. Energy Mater. Sol. Cells* **2013**, *119*, 73.

[32] S. Kim, J. a. Cianfrone, P. Sadik, K.-W. Kim, M. Ivill, D. P. Norton, *J. Appl. Phys.* **2010**, *107*, 103538.

[33] H. Yanagi, J. Tate, S. Park, C. H. Park, D. A. Keszler, *Appl. Phys. Lett.* **2003**, *82*, 2814.

[34] M.-L. Liu, F.-Q. Huang, L.-D. Chen, Y.-M. Wang, Y.-H. Wang, G.-F. Li, Q. Zhang, *Appl. Phys. Lett.* **2007**, *90*, 072109.

[35] D. Huang, Y.-J. Zhao, R.-Y. Tian, D.-H. Chen, J.-J. Nie, X.-H. Cai, C.-M. Yao, *J. Appl. Phys.* **2011**, *109*, 113714.

[36] J. Wang, *Mater. Today* **2007**, *10*, 55.

[37] K. Yang, M. Ichimura, *Jpn. J. Appl. Phys.* **2011**, *50*, 40202.

[38] K. Yang, Y. Nakashima, M. Ichimura, *J. Electrochem. Soc.* **2012**, *159*, H250.

[39] M. Dula, K. Yang, M. Ichimura, *Semicond. Sci. Technol.* **2012**, *27*, 125007.

[40] A. M. Yıldırım, *Opt. Commun.* **2012**, *285*, 1215.

[41] D. E. Ortíz-Ramos, L. A. González, R. Ramirez-Bon, *Mater. Lett.* **2014**, *124*, 267.

[42] S. H. Mohamed, *J. Phys. D: Appl. Phys.* **2010**, *43*, 035406.

[43] C. Corrado, J. K. Cooper, M. Hawker, J. Hensel, G. Livingston, S. Gul, B. Vollbrecht, F. Bridges, J. Z. Zhang, *J. Phys. Chem. C* **2011**, *115*, 14559.

[44] B. Car, S. Medling, C. Corrado, F. Bridges, J. Z. Zhang, *Nanoscale* **2011**, *3*, 4182.

[45] C. Corrado, J. K. Cooper, J. Z. Zhang, *Sci. Adv. Mater.* **2012**, *4*, 254.

[46] A. A. Khosravi, M. Kundu, L. Jatwa, S. K. Deshpande, U. A. Bhagwat, M. Sastry, S. K. Kulkarni, *Appl. Phys. Lett.* **1995**, *67*, 2702.

[47] A. M. Diamond, L. Corbellini, K. R. Balasubramaniam, S. Chen, S. Wang, T. S. Matthews, L.-W. Wang, R. Ramesh, J. W. Ager, *Phys. Status Solidi* **2012**, *209*, 2101.

[48] R. Downs, *Progr. Abstr. 19th Gen. Meet. Int. Mineral. Assoc. Kobe, Japan* **2006**, *3*, O03–13.

[49] F.-Q. Huang, M.-L. Liu, C. Yang, *Sol. Energy Mater. Sol. Cells* **2011**, *95*, 2924.

[50] H. Hiramatsu, K. Ueda, H. Ohta, M. Hirano, T. Kamiya, H. Hosono, *Appl. Phys. Lett.* **2003**, *82*, 1048.

[51] A. N. Banerjee, C. K. Ghosh, K. K. Chattopadhyay, *Sol. Energy Mater. Sol. Cells* **2005**, *89*, 75.

[52] H. M. Pathan, J. D. Desai, C. D. Lokhande, *Appl. Surf. Sci.* **2002**, *202*, 47.

[53] D. Lowndes, D. Geohegan, A. Puretzky, *Science* **1996**, *273*, 898.

[54] A. Ohtomo, M. Kawasaki, *Appl. Phys. Lett.* **1998**, *72*, 2466.

[55] S. Choopun, R. D. Vispute, W. Yang, R. P. Sharma, T. Venkatesan, H. Shen, *Appl. Phys. Lett.* **2002**, *80*, 1529.

[56] S. Pham, G. Barkema, L. Wang, *Phys. Chem. Chem. Phys.* **2015**, *17*, 26270.

[57] E. Fortunato, P. Barquinha, R. Martins, *Adv. Mater.* **2012**, *24*, 2945.

[58] M. Budnar, *Nucl. Instrum. Methods Phys. Res.* **1989**, *42*, 122.

[59] ICDD, *Powder Diffraction File Inorganic and Organic Data Book*, International Centre for Diffraction Data, Newtown Square, PA, USA, **2010**.

[60] C. F. Windisch, K. F. Ferris, G. J. Exarhos, *J. Vac. Sci. Technol., A* **2001**, *19*, 1647.

[61] S. Park, D. A. Keszler, M. M. Valencia, R. L. Hoffman, J. P. Bender, J. F. Wager, *Appl. Phys. Lett.* **2002**, *80*, 4393.

[62] K. H. L. Zhang, Y. Du, A. Papadogianni, O. Bierwagen, S. Sallis, L. F. J. Piper, M. E. Bowden, V. Shutthanandan, P. V Sushko, S. a Chambers, *Adv. Mater.* **2015**, *27*, 5191.